Production of Metallic Tungsten and Tungsten Carbide from Natural Wolframite and Scheelite *via* Sulfide Chemistry

CHARLES BOURY, SIERRA R. GREEN, and ANTOINE ALLANORE

The development of sulfide-based chemistry and physical separation in the last decade opens new processes to produce metals at the industrial scale. Herein, a new route to produce metallic tungsten and tungsten carbides particles from natural wolframite $(Fe,Mn)WO_4$ and scheelite $CaWO_4$ is presented. Sulfidation of mineral concentrates breaks the tungstate crystal structure into a mix of sulfides, in particular tungsten disulfide WS_2. The thermal instability of WS_2 at high temperature allows for its subsequent, selective, thermal reduction to tungsten particles at around 1500 °C. Similar thermal reduction in the presence of carbon result in the production of tungsten carbides, WC and W_2C, obtained at around 1250 °C. The other major components of the sulfidized concentrate remain un-reduced under the proposed conditions, demonstrating selective reduction of WS_2 as a possible new route for W recovery. Similar findings are reported for the carburization of WS_2.

I. INTRODUCTION

TUNGSTEN has a set of unique properties among metals, such as high melting point, low vapor pressure, high density, and high mechanical resistance. It has specific utilizations in spatial, military, and heavy-duty industrial applications where the use of tungsten, in a metallic or carbide form, is irreplaceable.[1] In 2020, the world mines production was around 84,000 metric tons of tungsten content, with more than 80 pct extracted in China.[2] Tungsten mines are usually of small size due to tungsten geographical dispersion and low concentration in the ore.[1] Wolframite $(Fe,Mn)WO_4$ and scheelite $CaWO_4$ are the main minerals processed. The conventional processing route described herein and shown in Figure 1 is a summary of the detailed work of Lassner *et al.* and Trasorras *et al.*,[1,3] sufficient to highlight the challenges of the incumbent processing technologies.

Ore beneficiation, presented in Figure 1 phase I, is required as most tungsten ores contains less than 1.5 wt pct equivalent tungsten oxide (WO_3). Natural ores are crushed and milled to liberate the particles of the tungsten containing minerals. Wolframite is concentrated by gravimetric and magnetic separation. Scheelite requires gravimetric and froth flotation methods. Pre-treatment by hydrochloric acid leaching and/or calcination may be necessary to decrease the presence of impurities such as arsenic, phosphorous, and sulfur and remove residual organic froth flotation agents. At that stage, oxidized cemented carbide scraps can be introduced for recycling. Next, untreated sodium tungstate (Na_2WO_4) is produced by a series of hydrometallurgical steps, chosen based on the feedstock mineralogy. Wolframite is digested by either concentrated sodium hydroxide (NaOH) or diluted NaOH under high pressure. Oxidized scraps are reintroduced for recycling in this stage. Scheelite requires a solution of sodium carbonate (Na_2CO_3) at high pressure to dissolve the concentrate. The solid-containing sludge resulting from this process is removed by filtration. The sludge is either disposed of, or further processed if it contains desirable elements.[4]

Phase II is the purification of the sodium tungstate solution and the formation of an ammonium isopolytungstate solution. It can be conducted either by liquid ion exchange (LIX) or by solid ion exchange (SIX). In the LIX-based process, aluminum sulfate and magnesium sulfate solutions are added in order to precipitate impurities such as silicates, phosphates, and fluorides. Magnesium salts and ammonium hydroxide are added for the removal of tin and arsenic. Molybdenum is removed by addition of sodium hydrosulfide (NaSH), forming thiomolybdate (MoS_4^{2-}), later precipitated as molybdenum sulfide (MoS_3). Tungsten is then extracted

CHARLES BOURY, SIERRA R. GREEN and ANTOINE ALLANORE are with the Department of Materials Science and Engineering, Massachusetts Institute of Technology, 77 Massachusetts Ave, Cambridge, MA 02139. Contact e-mail: allanore@mit.edu
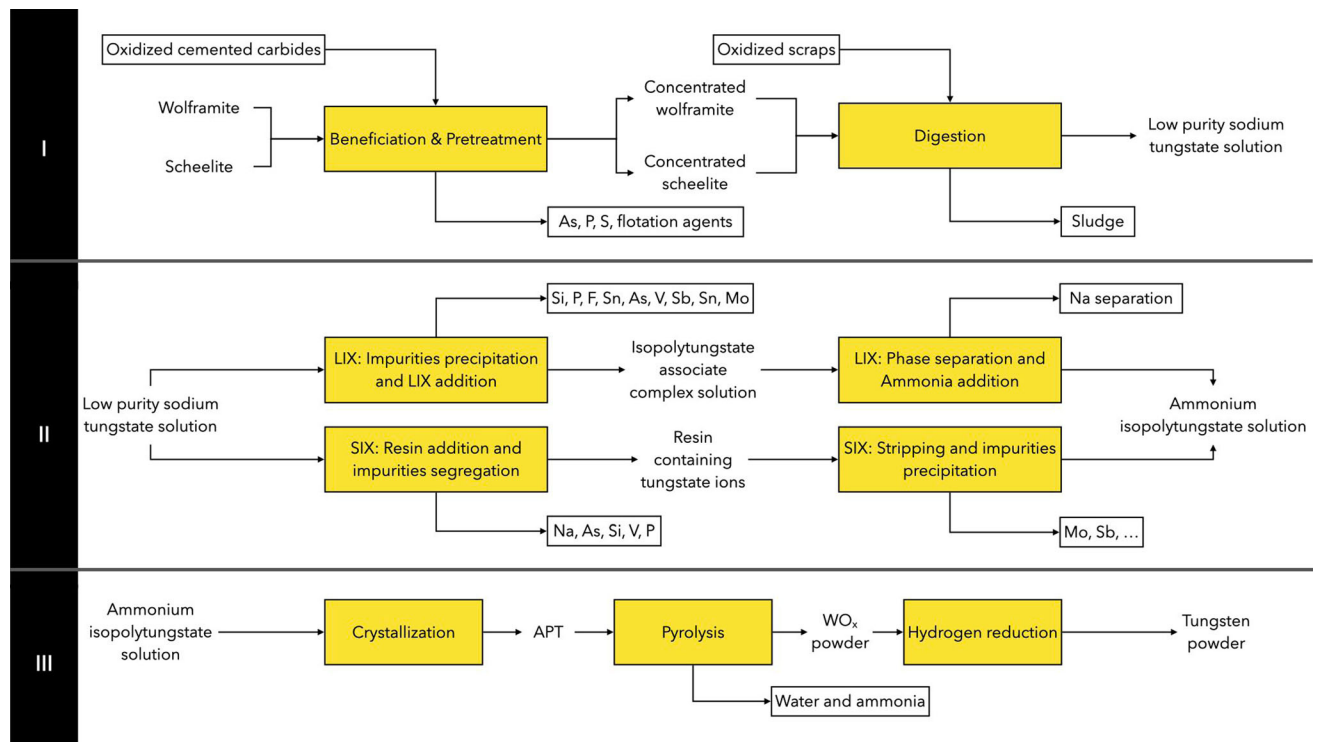
Fig. 1—Flowsheet of the established process of tungsten powder production[1,3] separated in three phases (I, II, III).

via liquid ion exchange as an isopolytungstate associate complex. The organic phase containing the isopolytungstate is extracted, washed, and mixed again with diluted ammonia to form an ammonium isopolytungstate solution. In the SIX-based process, the precipitation step is avoided, and a resin is directly added to selectively absorb tungstate anions. Silicon, vanadium, phosphorous, and arsenic are insoluble in the resin and therefore separated. Ammonium chloride (NH_4Cl) and ammonia (NH_3) solutions are added to strip the isopolytungstate solution. Molybdenum and other impurities are then removed with addition of ammonium sulfide (($NH_4)_2S$) and copper to form insoluble sulfides.

In phase III, the isopolytungstate solution is then evaporated and relatively pure crystalized ammonium paratungstate (APT) is formed. The crystallization process of APT only allows for few impurities to be entrained, making this process an important purification step. In a rotary furnace, the APT is pyrolyzed between 400 °C and 800 °C to evaporate water and ammonia while forming tungsten oxide. The chemical composition and micro-morphology of the oxide particles are function of the duration, temperature, and oxygen content. Yellow tungsten oxide WO_3 is formed when heating takes place in air, while a mix of blue tungsten oxides is formed under less oxidizing atmospheres. Hydrogen is then used to reduce the tungsten oxides powder to metal. The morphology and particle sizes (from 0.1 to 60 μm) of the reduced products is function of the temperature, duration, bed thickness, and the water vapor partial pressure.[5] In a pusher furnace above 600 °C and with a large excess of hydrogen,

tungsten oxide decomposes to tungsten and water vapor is formed and carried away by the excess hydrogen. The obtained tungsten powder is used afterward for powder metallurgy, metal injection molding, or other manufacturing processes.[6] The high temperature (> 2000 °C for several hours) required by powder metallurgy allows to further refine tungsten.[7]

Tungsten carbides WC and W_2C are the major products of the tungsten industry. In general, metallic tungsten particles are directly carburized between 1400 °C and 2000 °C under vacuum, nitrogen, or hydrogen.[8] Tschinkowitz, however, demonstrated that the carbon content of 6.1 wt pct (corresponding to WC) is only reached under hydrogen (H_2) or nitrogen (N_2) gasses.[9] The initial grain size and the processing parameters determine the final carbide powder grain size. Indeed, refining of large, grained powders is energetically intensive and modifies the carbon and oxygen contents, grain size, and shape. Other methods for tungsten carbide production consists in the carburization of tungsten oxide (WO_3)[10] or even natural scheelite ores ($CaWO_4$).[11] The two last methods, however, generate lower quality carbides. The production of sub-micron (up to 0.3 μm) tungsten carbides is also possible by solid gas reaction of sub-micron metallic tungsten with carbon containing gas such as CO[12] or CH_4.[8]

The actual process for tungsten metallic powder demonstrates several advantages: a relatively low temperature, a common process to convert sodium tungstate solutions (phase II and phase III of Figure 1), and the use of selective crystallization of APT to lower the impurity content. However, some limitations arise such as the need for calcination to handle Si, P, S, and F, the

need for hydrogen consumption for reduction, or the cost to permit the handling of the relatively hazardous chemicals. Issues are rising also from impurity management perspective, in particular molybdenum, calling for more calcination, froth flotation, or purification of sodium paratungstate. From an economical perspective, considering the high CAPEX and OPEX of the unit operations currently required to cope with environmental regulations, it is unclear whether processing capacity would easily be implemented in contemporary. This supports a renewed interest to consider the use of sulfidation combined with physical recovery,[13] which shows promising economy of scale from both a CAPEX/OPEX and environmental impact perspective. However, the authors could not find much prior art investigating the possible role of sulfur in the selective recovery and production of tungsten.

Prior studies on sulfidation cover a diverse range of chemistries and applications, from batteries recycling,[14] iron and copper refining,[15] and rare earth separation.[16] Amhad et al. demonstrated the sulfidation as a mean to enable separation of ilmenite and chromite.[17] Li et al. managed to treat low-grade lead-zinc oxide with elemental sulfur for flotation separation.[18] Zhang et al. used sulfide chemistry and HCl leaching to retrieve zinc from zinc-rich neutralization sludge.[19] Zinc was also selectively sulfidized in lead smelter slag by Zheng et al., Zheng et al., and Han et al.[20–22] Kaneko et al. demonstrated the synthesis of high-purity scandium sulfide from scandium oxide.[23] CS_2 and H_2S precursors have been widely used for their ease in transport through furnaces and thermodynamic features: low boiling point, high vapor pressure, and high reducing power. However, the control of selectivity is proved more difficult with such aggressive reagents[23–25] which often leads to undesirable side reactions. Ahmadi et al. demonstrated that the use of CS_2 as a sulfidizing agent resulted in the contamination of sulfide products with excess carbon.[26] Stinn et al. demonstrated that the use of gaseous elemental sulfur maximizes selectivity for individual sulfur products from mixed oxide feedstocks.[13] Industrially, the use of CS_2 represents a high risk in terms of safety[27] and requires specific precautions such as the use of stainless-steel vessels or water blanket. H_2S also presents a high toxicity and high flammability making these two reagents challenging for industrial applications.[28]

A new route to produce tungsten and tungsten carbide particles is presented herein. Previously, Stinn et al. demonstrated the sulfidation of pure tungsten oxide to WS_2 using elemental sulfur[13] but did not extend this approach to tungsten containing mineral feedstocks. Natural minerals of wolframite and scheelite were here utilized as feedstock. No chemical pretreatment was applied to remove impurities. The sulfidation of both tungstate crystal structures resulted in the formation of WS_2. The sulfidation of the wolframite showed a higher yield than the sulfidation of the scheelite in the same experimental conditions. The yield limitation for the scheelite conversion is discussed herein. The thermal reduction and carburization of WS_2 are presented as function of the partial pressure of

sulfur and temperature. The ability to obtain W or WC/ W_2C particles embedded in a mix of sulfides and oxides is demonstrated. Potential physical separation pathways to isolate tungsten products post-reduction or post-carburization are discussed. Molybdenum impurities, a growing challenge in tungsten purification, were not present in the tungsten feedstocks studied herein, but a thermodynamic discussion of the selective reduction of WS_2 in presence of MoS_2 is provided.

II. EXPERIMENTAL

Natural mineral rock samples are processed herein. The natural wolframite (139g, see Figure 2(a)) is obtained from the Hunan Province, China, while the natural scheelite (151g, see Figure 2(b)) is obtained from Guttannen, Switzerland. Both samples have been ground and sieved to 140 or 230 mesh (respectively, 105 and 63 μm maximum particle size) using an agate mortar and pestle and a stainless-steel sieve. Both rocks demonstrated relatively high elemental purity, and the detailed composition is presented later in the paper (see Table I). The wolframite sample is mainly composed of tungsten, manganese, iron, and oxygen. The scheelite sample is mostly composed of tungsten, calcium, and oxygen. Other elements are present but always at a content lower than 0.5 wt pct per element.

A. Thermodynamic of Sulfidation

Sulfidation reactions consist in breaking the tungstate structure, inherited from the W-O bonds to form a mixture of sulfides as shown for wolframite and scheelite in reactions [1] and [2].
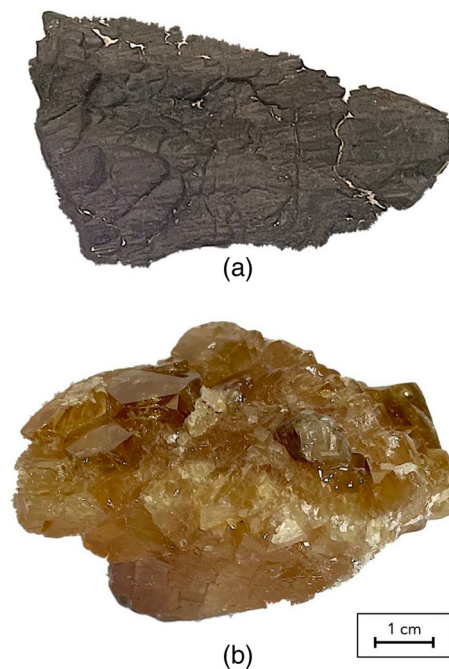

(a)

1 cm

(b)

Fig. 2—(a) Wolframite mineral; (b) Scheelite mineral.

Table I. ICP-AES and LECO (for O, S, C) Analytical Results, all in Wt Pct

Sample Type	W	Fe	Mn	Ca	Sn	Al	Cr	K	Mg	Nb	Si	Ti	Zn	O	S	C
Natural Wolframite	56.28	9.262	12.05	0.029	0.022	0.073	0.030	0.088	0.022	0.403	0.257	0.014	0.032	21.42	0.010	0.018
Sulfidized Wolframite	47.71	11.46	11.77	0.040	< 0.001	0.078	0.027	0.263	0.025	0.361	0.067	0.014	0.020	0.133	27.96	0.078
Natural Scheelite	63.66	0.069	0.167	12.88	< 0.001	< 0.001	0.036	0.137	< 0.001	0.024	0.088	0.002	0.027	22.89	0.004	0.015
Sulfidized Scheelite	61.11	0.100	0.037	12.53	< 0.001	< 0.001	0.035	0.292	< 0.001	0.019	0.090	0.003	0.025	9.021	16.70	0.039
Re-sulfidized Scheelite	58.54	0.081	0.029	11.75	< 0.001	< 0.001	0.034	0.320	< 0.001	0.019	0.098	0.003	0.024	3.426	25.62	0.051

$$(Fe, Mn)WO_{4(s)} + \frac{5}{2}S_{2(g)} \rightarrow WS_{2(s)} + (Fe, Mn)S_{(s)} + 2SO_{2(g)}$$

[1]

$$CaWO_{4(s)} + \frac{5}{2}S_{2(g)} \rightarrow WS_{2(s)} + CaS_{(s)} + 2SO_{2(g)} \quad [2]$$
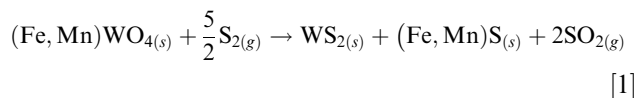
Figure 3 shows the S_2-SO_2 predominance diagrams of scheelite (considering an equimolar ratio W/Ca), tungsten oxide, and calcium oxide at a temperature of 1400 °C (data from FactSage 8.0, FactPS database, FactSage TM). The x-axis is the partial pressure of sulfur dioxide $SO_{2(g)}$ and the y-axis is the partial pressure of sulfur $S_{2(g)}$. No sulfates are considered for clarity purpose, as they are thermodynamically not expected to form in the temperature and oxygen range studied herein. The + line is the isobar at 1 atm ($p_{tot} = p_{SO_2} + p_{S_2} = 1$ atm). Following the isobar on the three systems, scheelite is expected to convert into a mix of sulfides for a ratio $p_{S_2}/p_{SO_2} = 10^2$ (red circle) while the sulfidation of tungsten oxide and calcium oxide happens for $p_{S_2}/p_{SO_2} = 10^{-1}$ and $p_{S_2}/p_{SO_2} = 10^{-2}$, respectively. Therefore, only WS_2 and CaS are stable in the conditions where the tungstate decomposes ($p_{S_2}/p_{SO_2} = 10^2$). This ratio of p_{S_2}/p_{SO_2} also transforms a tungstate (W: +6 valence) to a sulfide (W: +4 valence): the sulfidation reaction is therefore a partial reduction process of tungsten.

An equivalent discussion holds for wolframite, by analyzing the end members ferberite ($FeWO_4$) and hübnerite ($MnWO_4$). The ratios p_{S_2}/p_{SO_2} for the sulfidation of FeO to FeS and $FeWO_4$ to FeS and WS_2 are $p_{S_2}/p_{SO_2} = 10^{-2}$ and $p_{S_2}/p_{SO_2} = 10^1$, respectively. The ratios p_{S_2}/p_{SO_2} for the sulfidation of MnO to MnS and $MnWO_4$ to MnS and WS_2 are $p_{S_2}/p_{SO_2} = 10^{-1}$ and $p_{S_2}/p_{SO_2} = 10^1$, respectively. In both cases, the sulfide phases are stable in conditions where the tungstate decomposes. Thermodynamic information of $(Fe,Mn)WO_4$ and solid solution of $(Fe,Mn)S$ is, however, unknown.

B. Thermodynamic of Reduction and Carburization

With reactions [1] and [2] assumed to happen to completion following thermodynamic, the solids obtained after sulfidation are expected to contain a mixture of sulfides. The thermodynamic properties of the solid solutions of MnS and FeS: $(Fe,Mn)S$ are poorly understood and are therefore modeled using their separate end members. Reactions [3] through [6] represent the generic thermal decomposition reactions of the pure sulfides to metal and elemental sulfur, where solid, liquid, or gaseous metal-containing species could be present depending on the temperature.
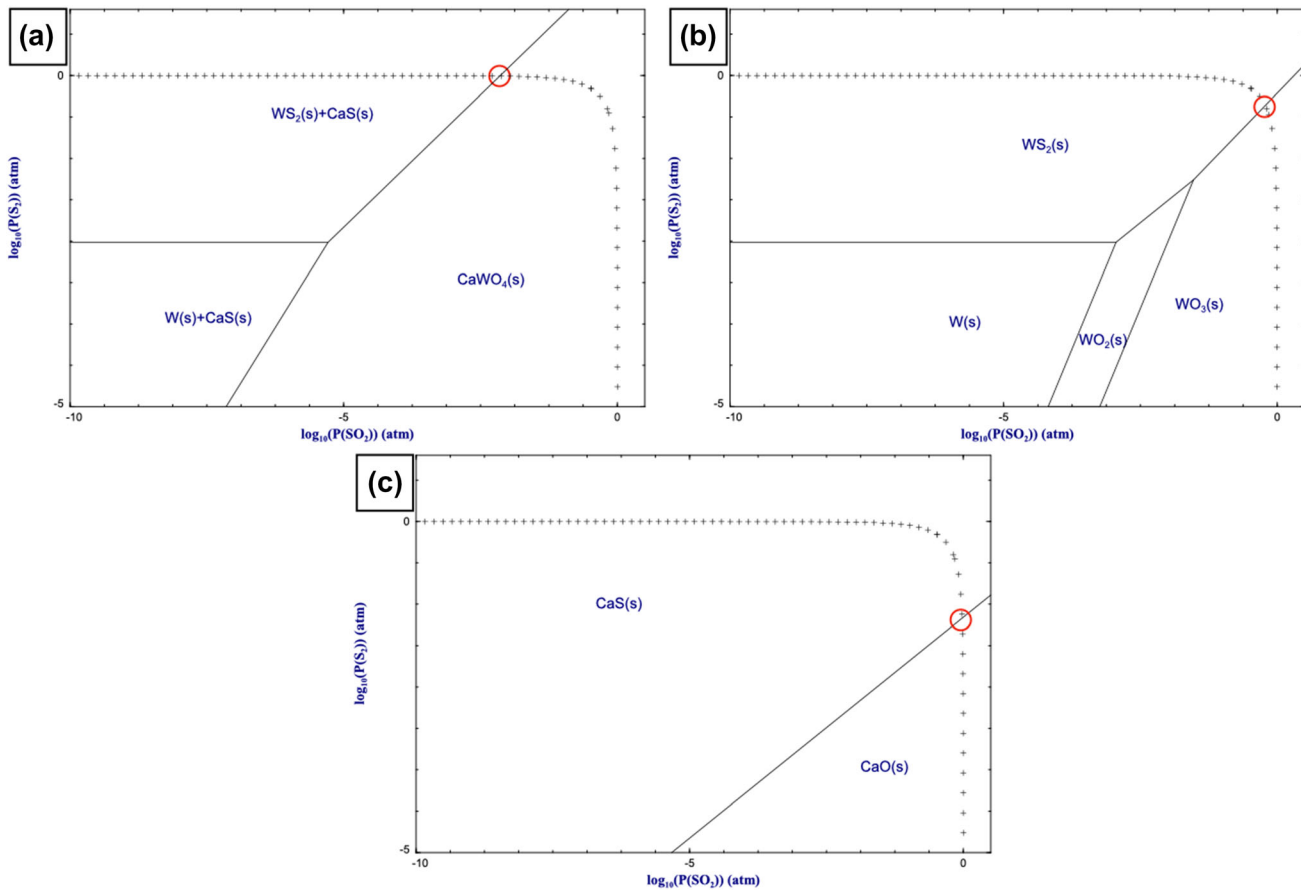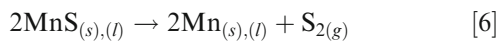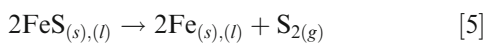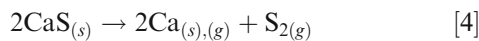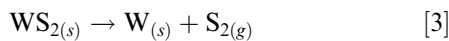
Fig. 3—Predominance diagram for (a) scheelite (considering an equimolar ratio W/Ca); (b) tungsten oxide; (c) calcium oxide; T = 1400 °C, + line is the isobar p_{tot} = 1 atm.

$$WS_{2(s)} \rightarrow W_{(s)} + S_{2(g)} \qquad [3]$$

$$2CaS_{(s)} \rightarrow 2Ca_{(s),(g)} + S_{2(g)} \qquad [4]$$

$$2FeS_{(s),(l)} \rightarrow 2Fe_{(s),(l)} + S_{2(g)} \qquad [5]$$

$$2MnS_{(s),(l)} \rightarrow 2Mn_{(s),(l)} + S_{2(g)} \qquad [6]$$

All thermodynamic data have been obtained from FactSage 8.0 using the FactPS database (FactSage TM) considering that high-temperature thermodynamic data of sulfides may be scarce or inaccurate. WS_2 exhibits two different crystal structures; however, thermodynamic data regarding their relative stability are limited.[29,30] Both crystal structures are assumed to be thermodynamically equivalent, and we therefore use its most common hexagonal crystal structure data. Sulfides such as WS_3, MoS_3, MnS_2, and Fe_7S_8 require high pressures of sulfur to form ($p_{S_2} > 1$ atm, FactPS database). They are therefore not considered herein. WS_2 and CaS do not have any solid–liquid phase transition data within the range of parameters ($T, p_{S_{2(g)}}$) used herein.

Figure 4 represents the Ellingham diagram for the reactions [3] through [6] per mole of S_2 as a function of the partial pressure of sulfur, considering the activities of solids, liquids, and CaS gas as unity and considering the reported condensed matter phase transitions included in the FactPS database. Table AI shows the detailed thermal decomposition reactions of the pure sulfides to metal and elemental sulfur within the temperature range from 1000 °C to 2000 °C and $p_{Ca(g)} = p_{S_{2(g)}} = 1$ atm.

Figure 4 shows the anticipated strong effect of the partial pressure of sulfur depending on the temperature, helping to define the most suitable process conditions for selective production of W. MnS and CaS demonstrate high stability even under very low partial pressure of sulfur. The decomposition temperature for WS_2 and FeS can be close to 1000 °C for a very low partial pressure of sulfur ($p_{S_2} = 10^{-6}$ atm). However, the temperature range for selective reduction of W is extended with increasing sulfur partial pressure. At a sulfur partial pressure of 10^{-2} atm, pure WS_2 is expected to thermally decompose into W and S_2 at 1500 °C while FeS is stable up to 2000 °C. Varying the partial pressure of $Ca_{(g)}$ from 1 to 10^{-6} atm does not change the order of stability of the sulfides significantly. For a partial pressure of $Ca_{(g)}$ of 10^{-6} atm and a partial pressure of $S_{2(g)}$ of 10^{-6} atm, the temperature for thermal decomposition of CaS is 1650 °C, largely above the temperature required for the thermal decomposition of WS_2 (1015 °C for $p_{S_2} = 10^{-6}$ atm).
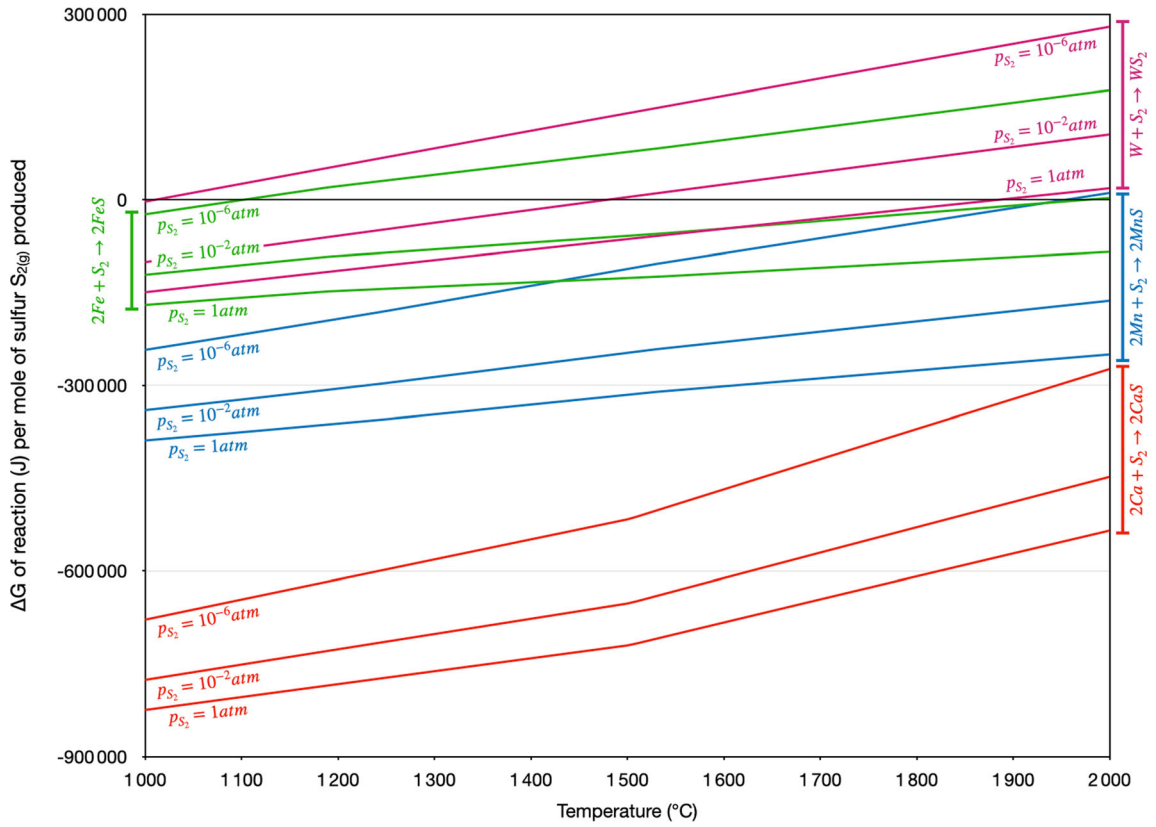
Fig. 4—Ellingham diagram for the sulfides of interest, considering different partial pressure of $S_{2(g)}$.

Similar analysis is proposed in the presence of carbon, leading to the formation of carbides WC, W_2C, CaC_2, Fe_3C, Mn_3C, and Mn_7C_3 from sulfides in Eqs. [7] through [12].
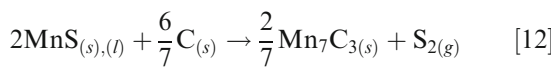
$$WS_{2(s)} + C_{(s)} \rightarrow WC_{(s)} + S_{2(g)} \qquad [7]$$

$$WS_{2(s)} + \frac{1}{2}C_{(s)} \rightarrow \frac{1}{2}W_2C_{(s)} + S_{2(g)} \qquad [8]$$

$$2CaS_{(s)} + 4C_{(s)} \rightarrow 2CaC_{2(s)} + S_{2(g)} \qquad [9]$$

$$2FeS_{(s),(l)} + \frac{2}{3}C_{(s)} \rightarrow \frac{2}{3}Fe_3C_{(s)} + S_{2(g)} \qquad [10]$$

$$2MnS_{(s),(l)} + \frac{2}{3}C_{(s)} \rightarrow \frac{2}{3}Mn_3C_{(s)} + S_{2(g)} \qquad [11]$$

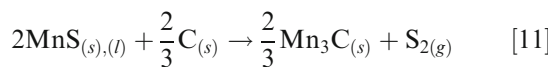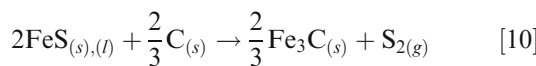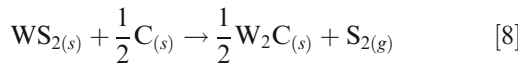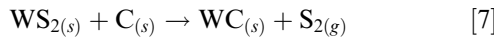$$2MnS_{(s),(l)} + \frac{6}{7}C_{(s)} \rightarrow \frac{2}{7}Mn_7C_{3(s)} + S_{2(g)} \qquad [12]$$

Table AII shows the detailed carburization reactions of the pure sulfides with carbon to carbides and elemental sulfur within the temperature range from 1000 °C to 2000 °C and $p_{S_2} = 1$ atm. Figure 5 represents the Ellingham diagram of the Eqs. [7] through [12] per mole of S_2 for different partial pressure of S_2, considering the activities of solids and liquids as unity and considering phase transitions. These data have also been obtained *via* FactSage 8.0 using the FactPS database.

A strong dependence on the sulfur partial pressure is expected for the production of a high-purity metal depending on the temperature of reaction. The carburization temperature for WS_2 and FeS can be close to 1000 °C at a very low partial pressure of sulfur (10^{-6} atm). The selectivity range is increasing with the increase of partial pressure of sulfur. At a sulfur partial pressure of 10^{-2} atm, WS_2 and C thermally carburize into WC or W_2C at 1300 °C while almost 2000 °C is required for FeS to react into Fe_3C. MnS and CaS again demonstrate high stability even under low partial pressure of sulfur. It must be noted here that WC is thermodynamically more favorable than W_2C.

C. *Sulfidation*

The sulfidation furnace used herein is similar in design to the one described by Stinn *et al.*[13] EDM grade graphite trays (Graphite Store, Northbrook, IL 60062) were custom-made. After machining, the crucibles were sonicated in acetone and dried in a vacuum oven for several hours. 100 g of sulfur powder (99.5 pct sublimed,
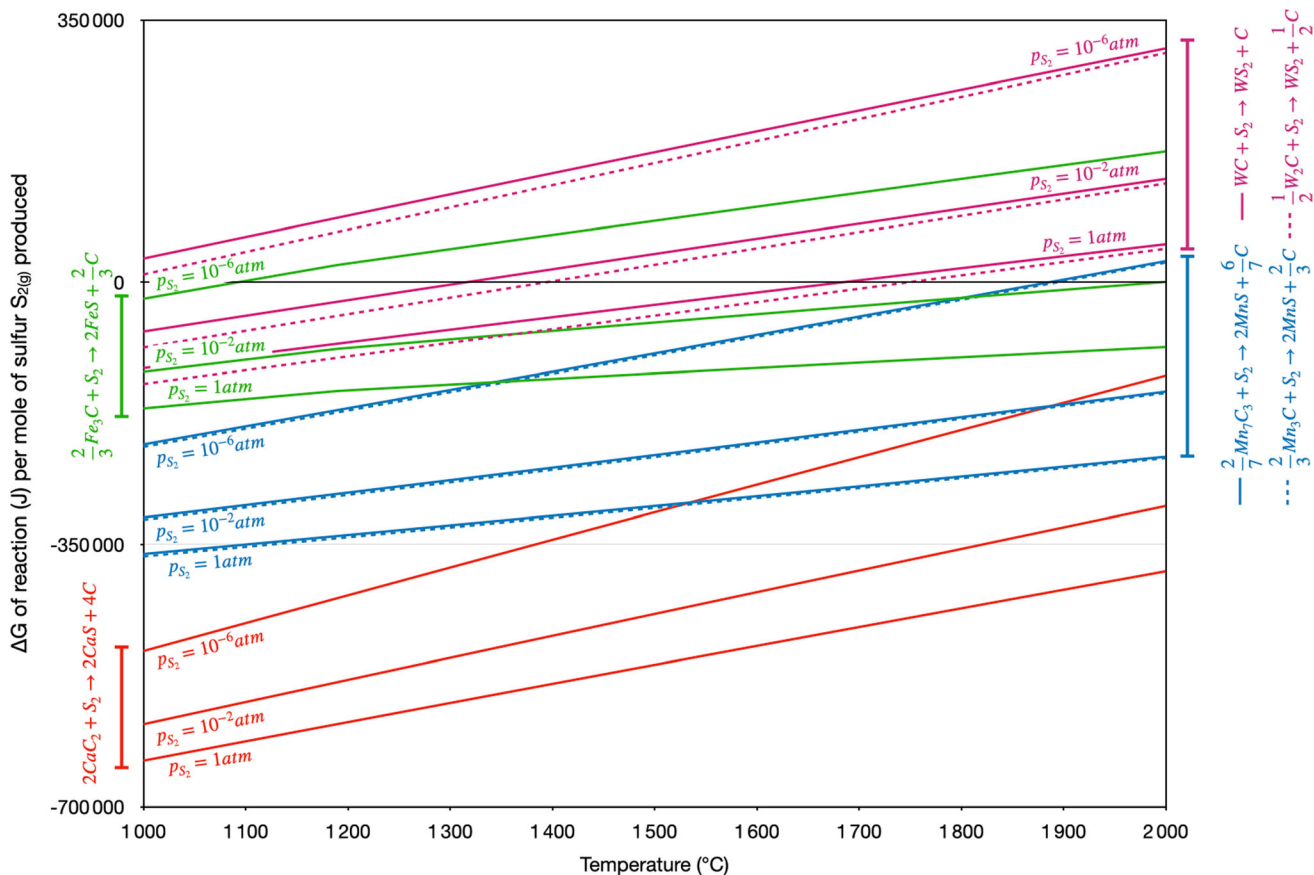
Fig. 5—Ellingham diagram of the carburization reactions of the sulfides of interest, considering different partial pressure of $S_{2(g)}$.

Acros organics, CAS 7704-34-9) was melted and cooled down in a quartz crucible and then loaded at the bottom of the furnace. Under 400 sccm of ultra-high-purity argon flow (UHP Ar, less than 10 ppm O_2, AirGas) in an alumina tube, the temperature was raised from room temperature to the targeted temperature at 3 °C per minute, then held at the targeted temperature for 2 hours, and then cool down at − 3 °C per minute to room temperature. The sulfur crucible was raised by 0.5 cm every 5 minutes during the first hour at targeted temperature. The pressure in the reactor did not exceed 1 atm. Several temperatures, particles sizes, and powder bed thickness have been experimented. Only the reactions with highest conversion yield are presented herein. The sulfidation yield ϕ is defined herein as the ratio of final sulfur concentration over the final concentration of anions of interest (S, O):$\phi = $ (final wt pct S)/(final wt pct S + final wt pct O).

The reduction or carburization steps to form metallic tungsten particles and tungsten carbide particles were conducted on two sulfidized samples. The first one is designated as « *wolframite with highest conversion yield* », the second one is denominated as « *scheelite with highest conversion yield* ». The sulfidized wolframite has been obtained after 2 hours at 1400 °C in a graphite crucible loaded in an alumina tube. The initial powder size was below 230 mesh (63 μm maximum particle size), and the bed thickness was around 1 cm. For the scheelite, two

sulfide samples have been produced for extensive analysis. One has been sulfidized once in the same conditions as wolframite above. The second sample has been sulfidized twice in the same conditions. Between the two sulfidation steps, the powder was re-crushed at 230 mesh in a glove box (less than 10 ppm H_2O). This product from the second sulfidation step of scheelite is the « *scheelite with highest conversion yield* ».

D. *Metallic Tungsten Production*

A container-less thermal imaging furnace (High-Temperature Xenon Lamp furnace, Model TX-12000-I) was employed to produce metallic tungsten. Samples were prepared in a similar fashion as the one presented in the previous work.[31] The sulfidized sample powders were compacted as rods of about 6 mm in diameter and 5 cm in length. Each rod would then hold in the center of the furnace. The furnace tube was evacuated to a pressure of 10^{-3} atm and re-purged with UHP Ar three times. Then 200 sccm of UHP Ar was flowed continuously. The hot zone of the furnace is around 1 cm^3 and the thermal gradient can reach several hundreds of degrees per centimeter. The sample could rotate at a speed of 6 rpm during a defined amount of time. The temperature could not be monitored due to the solid form of the sample. The oxygen concentration, below 9 ppm, was monitored by an oxygen analyzer (Advanced Micro Instruments,

Model 2001RS/RSP). Samples of, respectively, 5 and 3 grams of sulfidized wolframite and scheelite with highest conversion yield were used for the experiments.

In order to assess the thermal decomposition of WS_2, the minimal temperature required to observe the sulfur evolution of reaction [3] was determined in an induction tube furnace (UltraFlex UPT M35/150, HS-35/150, coil ID: 100 mm, coil height: 100 mm), apparatus similar in design to the one described by Stinn et al.[32] A graphite stand (OD: 40 mm, ID: 30 mm, height: 20 mm, GraphiteStore) was held on an alumina tube (OD: 35 mm, ID: 30 mm, height: 400 mm) and positioned within the center of a quartz furnace tube (OD: 50 mm, ID: 46 mm, height: 600 mm, Technical Glass Products, Painesville, OH 44077) sealed with vacuum fittings (ISO KF50, McMaster Carr) on each end. A tungsten crucible (OD: 30 mm, ID: 20 mm, height: 15 mm) was positioned on the top of the graphite stand. The furnace tube was positioned so that the tungsten crucible was aligned in the center of the induction coil. The same tungsten crucible was cleaned between each experiment with a diamond drill bit and sonicated in acetone prior use. The furnace tube was evacuated to a pressure of 10^{-3} atm and re-purged with UHP argon three times, then 2000 sccm of UHP Ar was flowed from the bottom of the reactor and evacuated through the top cap. During the experiment, the temperature was monitored using a type C thermocouple in direct contact with the bottom of the tungsten crucible. The tungsten crucible was heated to a set temperature over the course of 15 min and held at temperature while off-gassing was observable. Passed this time, the furnace was shut down and the sample cooled down naturally. Off-gas was observed around 1500 °C for both samples. Precise determination of the temperature of thermal decomposition is difficult as type C thermocouple cannot contact directly the sulfidized wolframite or sulfidized scheelite powders.

E. Tungsten Carbide Production

In the same induction tube furnace, a graphite crucible (OD: 39 mm, ID: 35 mm, height: 95 mm, GraphiteStore) replaced the tungsten crucible and graphite stand. Two identical graphite crucibles were custom machined for both experiments, The crucibles were sonicated in acetone and dried several hours in a vacuum oven at 200 °C prior use. The furnace tube was positioned so that the graphite crucible was aligned in the center of the induction coil. During the experiment, the temperature was monitored using a type C thermocouple in direct contact with the bottom of the graphite crucible. UHP Ar was flowed from the bottom of the reactor and evacuated through the top cap.

4 and 2.5 g of wolframite and scheelite, respectively, samples with highest conversion yield were used in the induction furnace experiments. Each powder had a maximum particle size of 63 μm (230 mesh size). The furnace tube was evacuated to a pressure of 10^{-3} atm and re-purged with UHP argon three times, then 2000 sccm of UHP argon was flowed during the experiment. The graphite crucible was heated to a temperature of 1600 °C over the course of 10 minutes and held at

temperature. The operating time at temperature was 15 minutes for 4 g of sulfidized wolframite and 10 minutes for 2.5 grams of sulfidized scheelite. Passed this time, the furnace was shut down and the sample cooled down naturally. Off-gas was observed around 1250 °C for both samples. Precise determination of the temperature of thermal decomposition is difficult as type C thermocouple cannot contact directly the sulfidized wolframite or sulfidized scheelite powders.

F. Characterization

The natural wolframite, natural scheelite, and their sulfides with highest conversion yield have been analyzed by Induction-Coupled Plasma—Atomic Emission Spectroscopy (ICP-AES, Applied Technical Services, 1049 Triad Court, Marietta, GA 30062), LECO combustion (Applied Technical Services, 1049 Triad Court, Marietta, GA 30062), and X-ray diffraction (XRD, PANalytical X'Pert Pro XRPD, MIT MRL facilities, MA, 02139).

To define the limiting step of the sulfidation for both wolframite and scheelite, the resulting sulfide powders have been cast in epoxy. High-resolution EDS maps (1024 pixels x 768 pixels) have been run to determine the semi-quantitative atomic concentration. The EDS detector (EDS, Sirius SD detector, SGX Sensor-tech Ltd.) is mounted on a scanning electron microscope (SEM, JEOL JSM- 6610LV, JEOL Ltd.).

Samples containing metallic tungsten and tungsten carbide particles were analyzed by X-ray diffraction and elemental analysis was conducted with a scanning electron microscope (SEM, JEOL JSM 7900F Schottky FE-SEM, JEOL) equipped with energy-dispersive spectroscopy detector (EDS, Oxford Ultim Max EDS Detector; Oxford Instruments) and wavelength-dispersive spectroscopy microprobes (WDS, Oxford Wave WDS detector, Oxford Instruments). EDS or WDS quantification of light elements such as O is proven less reliable than LECO. The carbon content is not available as carbon coating was applied for EDS/WDS quantification. EDS results of oxygen contamination are presented, and other elements (W, Ca, Mn, Fe, S) were quantified by WDS for a higher precision. All samples have been polished up to 0.25 μm with kerosene (Sigma Aldrich, reagent grade, low odor, CAS number 8008-20-6).

III. RESULTS AND DISCUSSION

A. Sulfidation Parameters

Figure 6(a) shows the initial scheelite and wolframite powders in the graphite trays, with their characteristic white and brown colors, respectively. Figure 6(b) is a typical result post-sulfidation, and no color difference is observable between the sulfidized wolframite and scheelite when the sulfidation yield is high ($\phi > 80$ pct). Table I presents the ICP-AES and LECO composition of natural wolframite, natural scheelite, sulfidized wolframite, single sulfidized scheelite, and doubly sulfidized
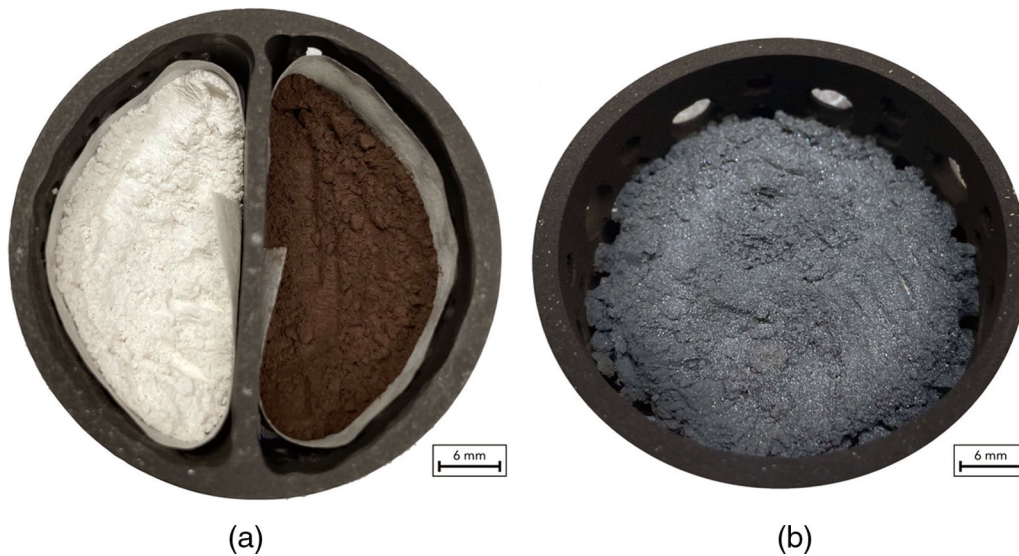
Fig. 6—(a) Graphite crucible containing separated powders of scheelite (left) and wolframite (right) ground to 230 mesh; (b) sulfidized wolframite with highest conversion yield.

scheelite with highest conversion yield. The amount of oxygen left in the doubly sulfidized scheelite is 3.426 wt pct, compared to 0.133 wt pct for the sulfidized wolframite. The sulfidation yield for wolframite is $\phi = 99.53$ pct, and the sulfidation yields of the single and doubly sulfidized scheelite are $\phi = 64.93$ pct and $\phi = 88.00$ pct, respectively. Among the other elements analyzed, the carbon content increases only slightly (0.018 to 0.078 wt pct for wolframite and 0.015 to 0.051 wt pct for scheelite). The graphite crucibles may contain small carbon powder ending up in the resulting sulfides mix. Tin oxide is absent from the sulfidized wolframite, likely because it is expected to volatilize as tin sulfide which boils at 1274 °C and atmospheric pressure following FactSage (FactPS). The reliability of the ICP-AES results was found questionable because of the potential difficulty in dissolving tungstate minerals in hydrofluoric acid. Therefore, we do not know whether the variations of W, Fe, Mn, and Ca contents between the natural minerals and their respective sulfides are quantitative. The metal content variations (*e.g.*, Fe) from the oxide to the sulfide are expected to also suffer from a similar analytical method limitation. These elemental analyses were conducted only on a subsample of few milligrams. The reported concentrations of transition metals are therefore subject to sampling variations in the starting minerals and products.

For both minerals, the temperature, the thickness of the original powder bed, and the particle size have been observed to affect the sulfidation yield for a same operating time of 120 minutes at temperature. For both the wolframite and the scheelite, an increase of operational temperature leads to a large increase in yield. This trend is similar in direction to the one observed by Zhang *et al.* during the sulfidation of barium sulfate ($BaSO_4$)[33] or by Stinn *et al.* during the sulfidation of lanthanum oxide (La_2O_3).[13] However, no assumption or distinction between phase boundary reaction control (reaction limited) or product layer diffusion control

(diffusion limited) can be proposed such as in the work presented by Ahmad *et al.*[34] In the later, the sulfidation of natural chromite with diluted H_2S is studied and the kinetic of sulfidation is described by the Ginstling–Brounshtein model for diffusion-controlled mechanism. The work by Sohn *et al.*[35] describes the fluid–solid reactions in porous pellets where the effective diffusivity inter-grains is changing with the generation of product on the outer layer of the pellet. A slower diffusion of the sulfur fluid through the pellet would limit the reaction (fluid transport limited) in the core as described by Sohn *et al.*[36] following the law of additive reaction times for fluid–solid reactions. A large bed thickness may therefore be detrimental due to sintering effects at temperature and low penetration depth of the sulfur through the bed. Indeed, a cross-sectional color difference from the reaction front can be noticed when the powder bed was too thick (> 2 cm). The particle size seemed to have a greater effect for scheelite than wolframite, as explained later in this paper. For a same temperature, reducing the particle size by half (140 to 230 mesh) did not seem to affect the yield of sulfidation for the wolframite (sulfidation yield approximatively equivalent).

B. Sulfidation Effect on the Tungstate Crystal Structure

Figures 7(a) through (e) are the XRD results of the natural wolframite, sulfidized wolframite, natural scheelite, sulfidized scheelite, and doubly sulfidized scheelite, respectively. The XRD pattern of natural wolframite (Figure 7(a)) has been reported to be dependent of the ratio Fe/Mn; however, the actual level of resolution is insufficient to quantify this ratio.[37,38]

Regarding the solid solution of manganese sulfide and iron sulfide (Fe,Mn)S, the high amount of manganese in the starting materials (12.05 wt pct) leads to a solid solution based on MnS crystal structure. This is in agreement with the previously reported solubility of FeS
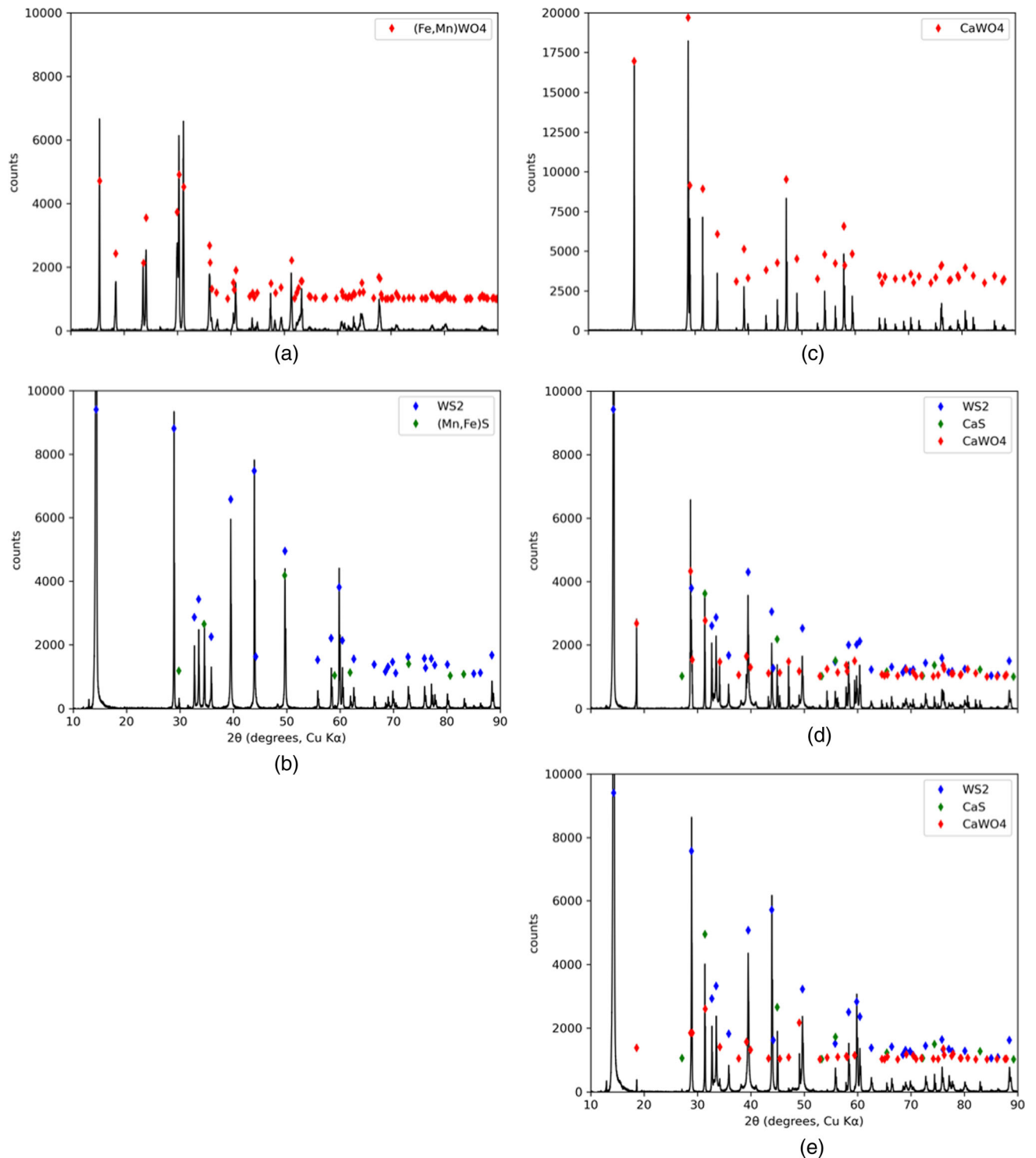
Fig. 7—XRD scans of (*a*) natural wolframite; (*b*) sulfidized wolframite with highest conversion yield; (*c*) natural scheelite; (*d*) single sulfidized scheelite with highest conversion yield; (*e*) doubly sulfidized scheelite with highest conversion yield.

in MnS as shown in the work of Knitter *et al.*[39] The sulfidized wolframite sample, in Figure 7(b), contains a mixture of WS_2 and a (Fe,Mn)S solid solution. The initial wolframite crystal structure is absent from the product, indicating the successful and complete

sulfidation (in terms of tungstate structure removal) of the wolframite sample. No other oxides are observed by XRD or EDS, and the residual oxygen noted in Table I is therefore dilute oxygen in the mix of sulfides.

The sulfidation of the scheelite is found to be incomplete. From Figures 7(c) through (e), it can be noticed that the initial calcium tungstate crystal structure is still found by XRD after the first and second sulfidation. The two new sulfide phases found post-sulfidation are WS_2 and CaS.

SEM images of the natural wolframite, sulfidized wolframite, natural scheelite, and doubly sulfidized scheelite are presented in Figure 8. With an initial maximum particle size of 63 μm, neither sintering nor particle growth is observed on the sulfidized samples. The newly formed sulfide phases exhibit polygonal shapes superposed on larger particles. These large grains are sulfides in the case of the wolframite (oxygen content of 0.133 wt pct) but contain the remaining calcium tungstate in the case of the scheelite (oxygen content of 3.426 wt pct).

C. Sulfidation Limiting Step

Table I indicates for each sample, the weight percent of oxygen left after sulfidation. The reaction can be considered almost complete for the wolframite since the remaining oxygen concentration is low (0.133 wt pct). However, for scheelite, one can notice the high level of oxygen even after two sulfidations (3.426 wt pct)

Figures 9, 10, and 11 show the sulfidized wolframite, sulfidized scheelite, and doubly sulfidized scheelite powders, respectively. All powders have been passed through a 230-mesh sieve prior analysis. Each figure contains an SEM/BEC image, a quantified "anionic" species molar ratio of [S]/[S+O], and a quantified "cationic" molar ratio of [W]/[W+Fe+Mn] or [W]/[W+Ca] as measured by EDS.

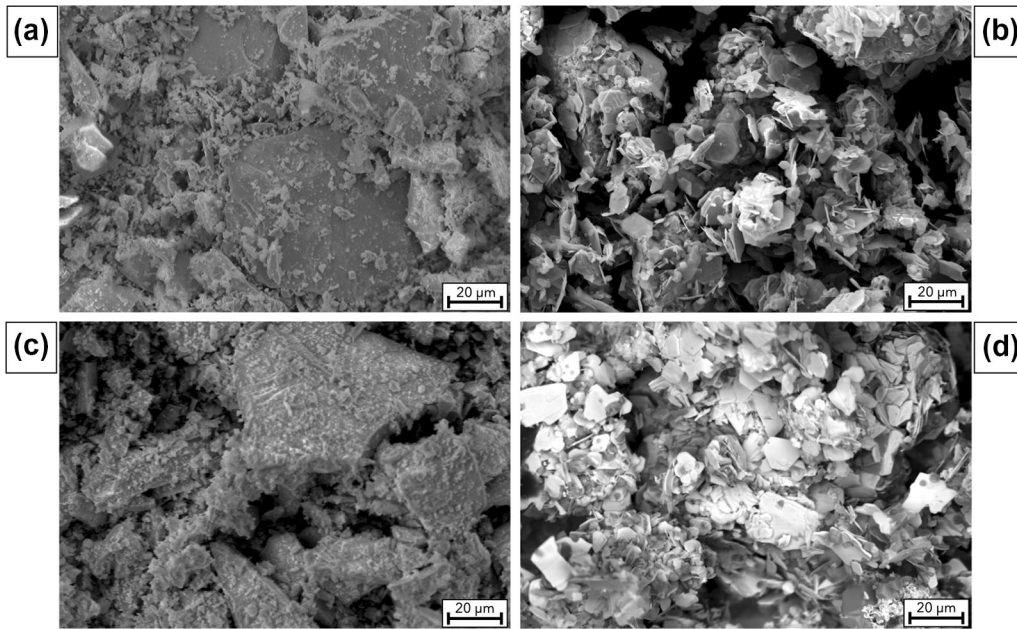Fig. 8—SEM images of (*a*) natural wolframite; (*b*) sulfidized wolframite with highest conversion yield; (*c*) natural scheelite; (*d*) doubly sulfidized scheelite with highest conversion yield.
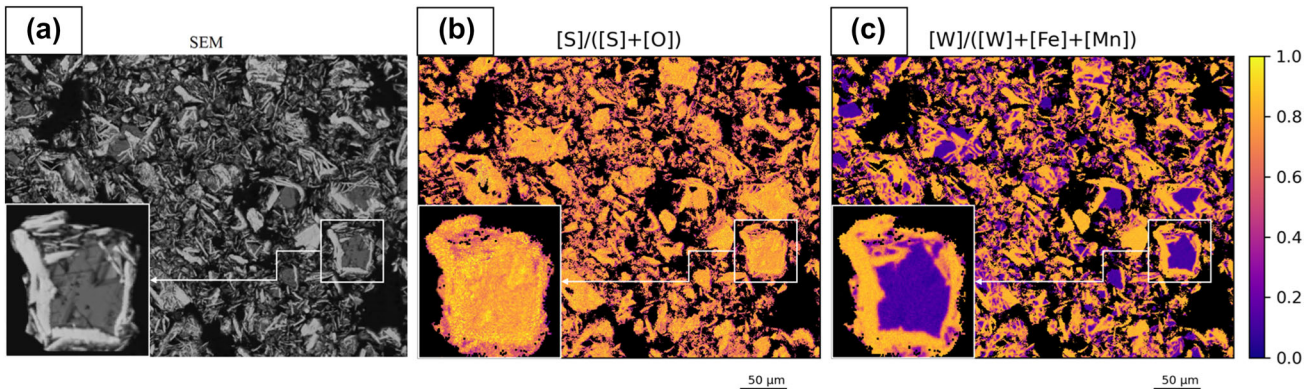

Fig. 9—(*a*) SEM/BEC image; (*b*) quantified "anionic" species molar ratio of [S]/[S+O]; (*c*) quantified "cationic" molar ratio of [W]/[W+Fe+Mn] as measured by EDS for sulfidized wolframite with highest conversion yield.

The sulfidized wolframite study (Figure 9) confirmed the high conversion yield ($\phi = 99.53$ pct). In combination with the XRD results where no other phases than sulfides are found, it suggests again that the oxygen remaining is diluted in the sulfide phases. Two colors are observable for the molar ratio of $[W]/[W + Fe + Mn]$ corresponding to WS_2 (bright yellow, cationic ratio near 1) and the solid solution of FeS and MnS (dark blue, cationic ratio near 0). These phases are also the only one observed in the XRD scan (see Figure 7(b)).

The single sulfidized scheelite (Figure 10) exhibits two colors on the $[S]/[S + O]$ map. Either a bright yellow color (anionic ratio near 1) or a dark blue color (anionic ratio near 0) is visible. The bright yellow represents sulfide phases such as WS_2 or CaS while the dark blue represents the oxide/scheelite phase $CaWO_4$. Similar analysis stands using the molar ratio of $[W]/[W + Ca]$. Three different colors are observed corresponding to WS_2 (bright yellow, cationic ratio near 1), CaS (dark blue, cationic ratio near 0), and $CaWO_4$ (orange, cationic ratio approximatively 0.5). These phases are also the only one observed in the XRD scan (see Figures 7(d) and (e)). It can be noticed that for most of the large grains, a yellow circle is surrounding a dark blue core indicating that the sulfide phases surround the oxide phase.

The doubly sulfidized scheelite (Figure 11) demonstrates similar features as the single sulfidized scheelite. The same phases are present in the XRD scan but the ratio of sulfide compounds (WS_2, CaS) to the initial scheelite ($CaWO_4$) is higher than for the single sulfidized one. This suggests that for scheelite, the sulfide phases are formed on the outside of the particles and the « sulfidation » makes its way from the surface to the core. This result can be compared to the work of Cho et al. and Sohn[40,41] where the use of a shrinking-core model supported the observed progress of conversion. More work is needed on tungstate sulfidation to verify if the mass transfer through the particles or the chemical reaction controls the overall sulfidation rate. The homogeneous model[42] considering intra-porosity of particles is less suitable as the halo of sulfides surrounding the oxide phase is sharp (see Figures 10(b) and 11(b)). The effect of bulk flow due to volume change in the gas phase on the gas–solid reaction[43] (consumption of S_2, formation of SO_2) could also be considered.[13]
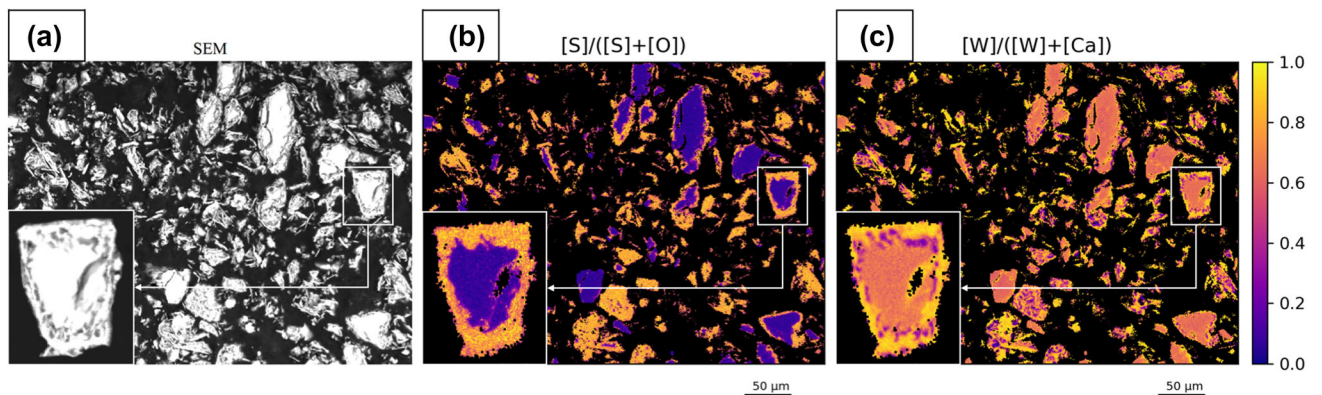

Fig. 10—(a) SEM/BEC image; (b) quantified "anionic" species molar ratio of $[S]/[S + O]$; (c) quantified "cationic" molar ratio of $[W]/[W + Ca]$ as measured by EDS for single sulfidized scheelite with highest conversion yield.
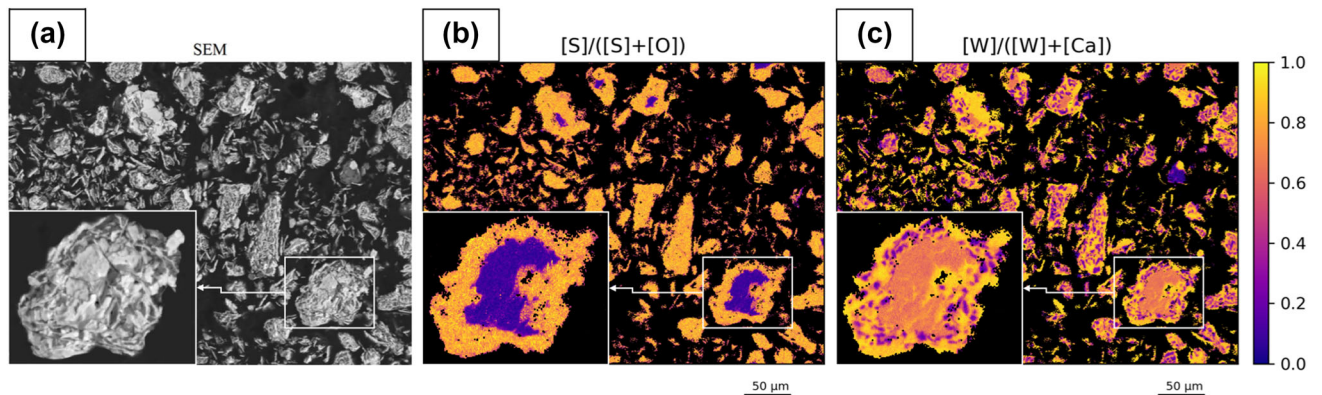

Fig. 11—(a) SEM/BEC image; (b) quantified "anionic" species molar ratio of $[S]/[S + O]$; (c) quantified "cationic" molar ratio of $[W]/[W + Ca]$ as measured by EDS for doubly sulfidized scheelite with highest conversion yield.

D. Metallic Tungsten Production

Figures 12(a) and (b) are, respectively, examples of a compacted sulfidized wolframite rod at the beginning and at the end of the thermal treatment inside a container-less Thermal Imaging Furnace. During the experiment, a large amount of gas evolved from the rod, and the sample was found to shrink over almost one hour at temperature. A shinny crust formed on the outside of the sample. After almost an hour at temperature, the experiment was stopped as the sample was not evolving in shape anymore and no more off-gas was visible. A part of the recovered sample was crushed for XRD analysis while another part was casted in epoxy for SEM and WDS detailed analysis.

The experiment on the doubly sulfidized scheelite exhibited less gas generation. Once the crust was formed on the outside, no more off-gas was visible. This can be due to either the optical reflectivity of the formed metallic crust or the low thermal conductivity of the calcium sulfide and calcium tungstate, both of which may affect the sample temperature in such optical furnace.

Figures 13(a) and (b) show, respectively, the XRD patterns of the sulfidized wolframite and doubly sulfidized scheelite with highest conversion yield after their thermal decomposition. Metallic tungsten peaks are present for the wolframite samples, though the conversion to metal did not reach completion as revealed by the presence of peaks attributed to WS_2. The solid solution of manganese and iron sulfide was not thermally decomposed. For the scheelite sample, the metallic tungsten pattern is visible but only to a small extent, suggesting a very limited advancement of the thermal decomposition. The initial scheelite crystal structure, calcium sulfide, and unreacted tungsten sulfide are observable via XRD. For both wolframite and scheelite,

the WS_2, (Fe,Mn)S solid solution, $CaWO_4$, and CaS XRD patterns are unchanged post-WS_2 thermal reduction.

Figure 14 presents the SEM images of the tungsten particles remaining in the samples from the reduction experiments of sulfidized wolframite and doubly sulfidized scheelite. In Figure 14(a), the light particles are metallic tungsten particles, while the darker phase is a mix of WS_2 and (Fe,Mn)S. In Figure 14(b), the light particles are metallic tungsten, the dark phase is the calcium sulfide, and the gray phase is a mix of calcium tungstate and tungsten sulfide. Table II presents the average concentration of the tungsten particles analyzed by EDS/WDS. The highest contaminant post-reduction is oxygen. Other elements are below 0.5 wt pct on average.

E. Tungsten Carbide Production

Figure 15 shows the XRD patterns of the carburization experiments of sulfidized wolframite and scheelite with highest conversion yield. One can notice the completion of the reaction in the case of the wolframite, where the WS_2 pattern is absent, and the (Fe,Mn)S peaks remain. In the case of the scheelite, a mix of WC and W_2C is observed in addition to CaS while $CaWO_4$ is no longer present. Reactions [13] and [14] are possible reactions involving scheelite. Both are thermodynamically favorable above 1000 °C for a partial pressure $p_{Ca} = p_{CO} < 10^{-2}$ atm and considering other activities as unity. Reaction [13] is, however, thermodynamically more favorable per mole of scheelite for a same partial pressure $p_{Ca} = p_{CO}$. No trace of CaC_2 is observed on XRD scan (Figure 15(b)) and EDS analysis. Reaction [13] therefore explains the absence of $CaWO_4$ on the resulting mixed powder.
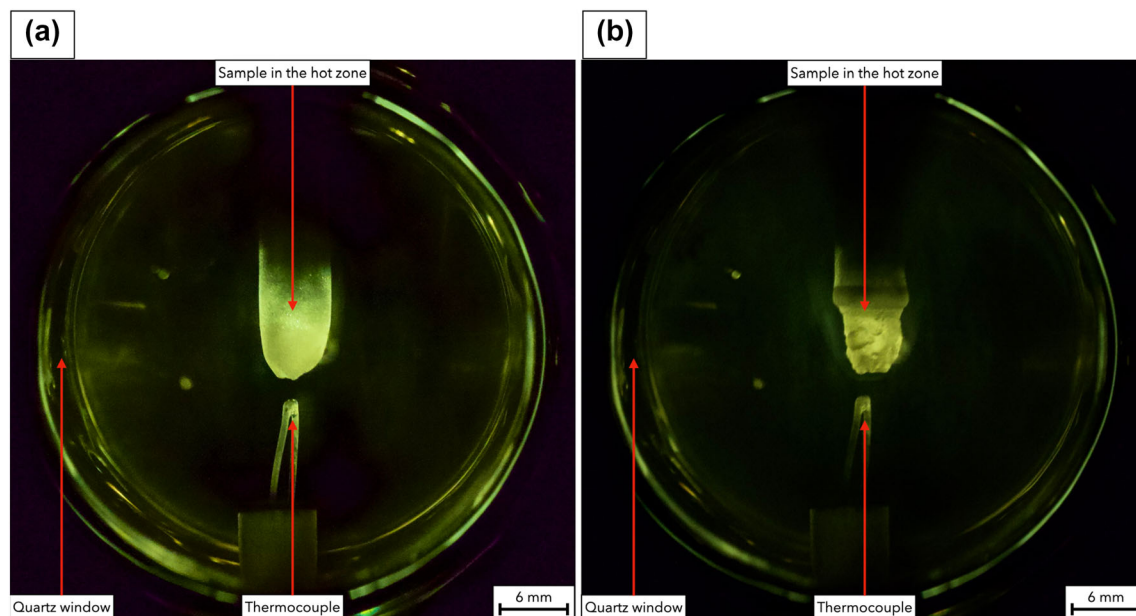

Fig. 12—Compacted sulfidized wolframite rod with the highest conversion yield (a) at the beginning; (b) at the end of the thermal treatment inside the Thermal Imaging Furnace.
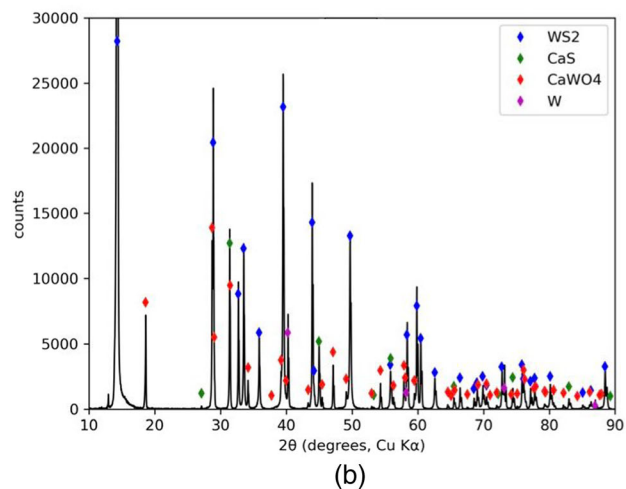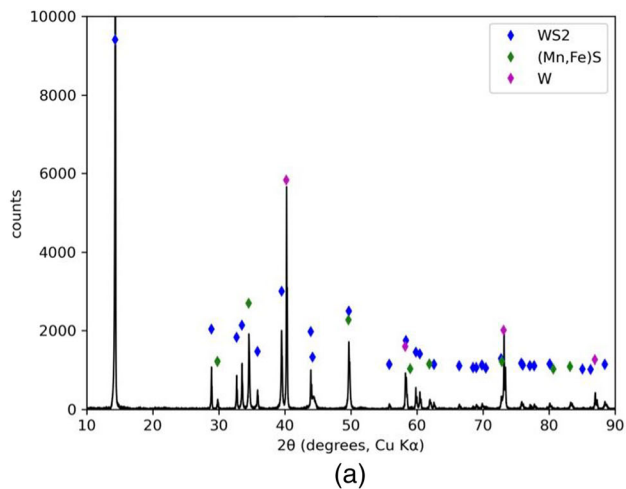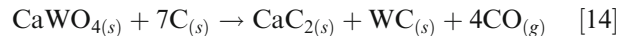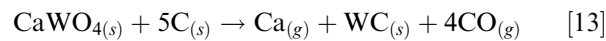
Fig. 13—XRD pattern post-thermal decomposition of (*a*) sulfidized wolframite with highest conversion yield; (*b*) doubly sulfidized scheelite with highest conversion yield.

$$CaWO_{4(s)} + 5C_{(s)} \rightarrow Ca_{(g)} + WC_{(s)} + 4CO_{(g)} \quad [13]$$

$$CaWO_{4(s)} + 7C_{(s)} \rightarrow CaC_{2(s)} + WC_{(s)} + 4CO_{(g)} \quad [14]$$

The presence of both WC and W_2C in the scheelite experiment could be explained by local deficiency of carbon at some locations in the solid reacting material. The carbon content is expected to originate from the graphite crucible; however, if the powder is not evenly spread and in a thin layer on the graphite crucible, some locations can be deficient in carbon, or the tungsten carbide formed in the early stage may block further reaction. Thermodynamically, one can notice on Figure 5 that for all temperatures and partial pressures of sulfur, the formation of WC is more favorable than W_2C.

Both carbides were analyzed by EDS and WDS analysis and the results are presented in Table II. The carbon content is not available. Again, the highest contaminant post-carburization is the oxygen. Other elements are below 0.25 wt pct on average.

F. *Potential Improvements and Discussion on the Sulfidation Step*

Thermodynamically, the sulfidation of wolframite or scheelite can be conducted at lower temperatures than demonstrated herein (*e.g.*, 1200 °C instead of 1400 °C). By LeChatelier principle, lower partial pressure of SO_2 (more reducing environment) is, however, required to increase further the thermodynamic driving force for the sulfidation reactions [1] and [2]. At lower temperatures, the kinetics of sulfidation may be slower and longer sulfidation times may be required, as observed during the sulfidation of La_2O_3 by Stinn *et al.*[13] Our results with scheelite suggest either a mass transfer limitation for sulfur through the particles or intrinsic kinetic
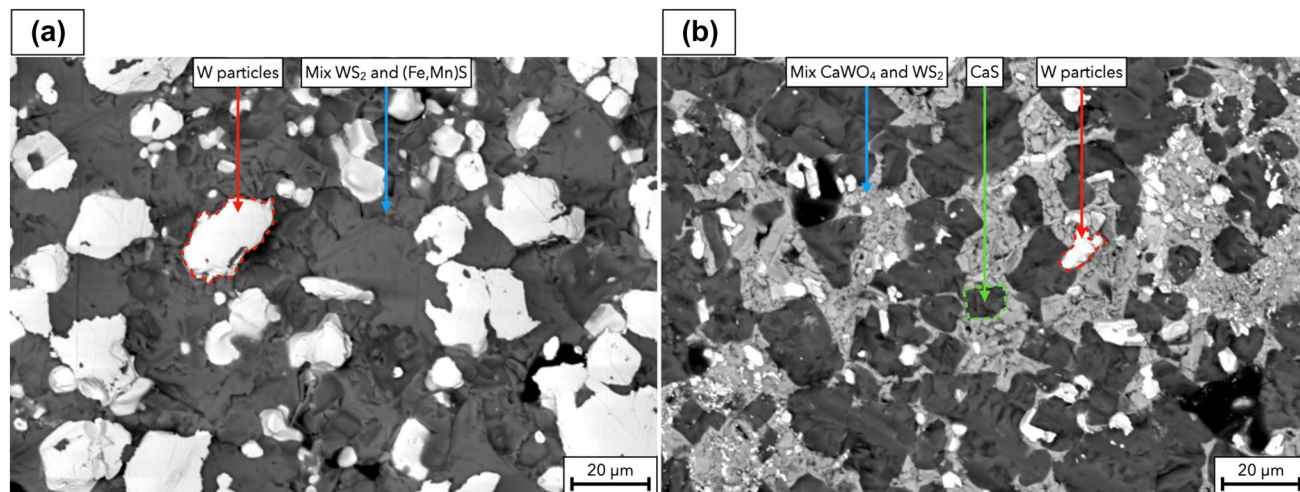

Fig. 14—SEM images of the tungsten particles remaining in the samples from the reduction experiments of (*a*) sulfidized wolframite with highest conversion yield; (*b*) doubly sulfidized scheelite with highest conversion yield.

Table II. Average Composition of the Analyzed Metallic Tungsten Particles, Values are in Wt Pct and Obtained *via* WDS Except for O Which Values are Obtained *via* EDS, C is not Quantified

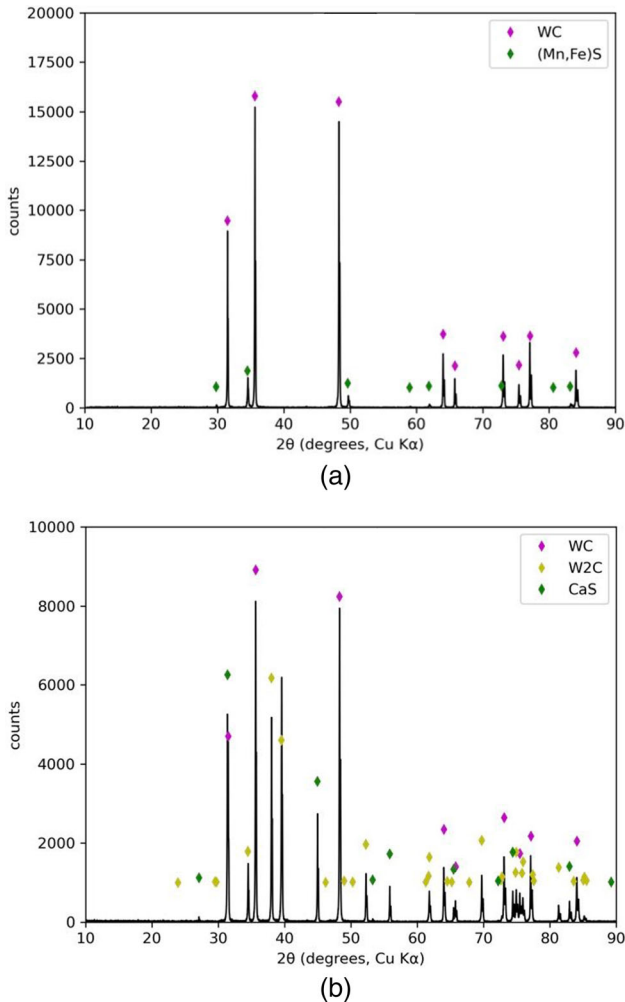| Sample Type	W	Fe	Mn	Ca	S	O
W from Sulfidized Wolframite	97.501	0.251	<0.001	—	0.229	2.019
W from Double Sulfidized Scheelite	97.600	—	—	0.302	0.379	1.719
WC from Sulfidized Wolframite	98.399	0.233	<0.001	—	0.250	1.118
WC and W_2C from Doubly Sulfidized Scheelite	98.486	—	—	0.103	0.095	1.317

Fig. 15—XRD patterns of the carburization experiments of (*a*) sulfidized wolframite with highest conversion yield; (*b*) doubly sulfidized scheelite with highest conversion yield.

limitation of the reaction. Sulfidation of scheelite may therefore benefit from a smaller particle size, which can be detrimental from a feedstock preparation standpoint: higher energetical requirements are needed for smaller particle sizes.[44] The improvement of sulfidation yield can possibly allow for a single pass conversion. Herein the reaction is studied in a batch, fixed bed configuration, but at scale, a rotary-type furnace could be used to alleviate the present fixed bed thickness and optimize gaseous sulfur flow during sulfidation.[45]

Other important parameters, not studied herein, are the partial pressure of sulfur, the argon carrier gas flow rate, and the amount of carbon in the system (graphite, alumina…). These parameters would play a key role in the sulfidation yield as described in the paper by Stinn et al.[13]

The use of more aggressive gas such as CS_2 and HS_2 could be considered due to the non-selectivity of the process. CS_2 use, however, has been found to increase the carbon content in the resulting sulfides.[26] It could be detrimental on the tungsten purity and potentially involves the formation of carbide when not desired.

G. Potential Improvements and Discussion on the Reduction and Carburization Step

Molybdenum, an important impurity in scheelite minerals,[46,47] was not present in the natural ore samples treated herein. This analysis does not consider the alloying of W and Mo or solid solutions containing Mo, W, and S,[48] suggesting that further work is required to fully evaluate the selectivity of the process with respect to Mo. Assuming that both tungstate WO_4^{2-} and molybdenate MoO_4^{2-} have similar sulfidation patterns (molybdate to molybdenum sulfide without oxide formation), it is possible to use the thermodynamic data available on FactSage, FactPS database for MoS_2, Mo_2S_3, and the molybdenum carbides Mo_2C and MoC. The reactions [3], [7], [15] through [18] are therefore considered, while other reactions, discarded for clarity, were found less favorable thermodynamically.
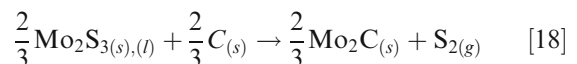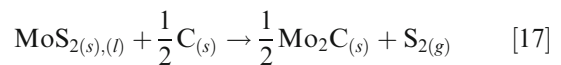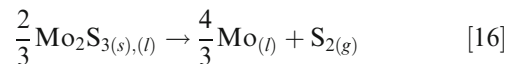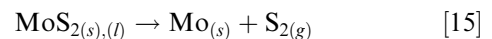
$$MoS_{2(s),(l)} \rightarrow Mo_{(s)} + S_{2(g)} \quad [15]$$

$$\frac{2}{3}Mo_2S_{3(s),(l)} \rightarrow \frac{4}{3}Mo_{(l)} + S_{2(g)} \quad [16]$$

$$MoS_{2(s),(l)} + \frac{1}{2}C_{(s)} \rightarrow \frac{1}{2}Mo_2C_{(s)} + S_{2(g)} \quad [17]$$

$$\frac{2}{3}Mo_2S_{3(s),(l)} + \frac{2}{3}C_{(s)} \rightarrow \frac{2}{3}Mo_2C_{(s)} + S_{2(g)} \quad [18]$$

Figure 16 represents the Ellingham diagram of WS_2, MoS_2, and Mo_2S_3 as a function of temperature for a partial pressure of S_2 of 10^{-2} atm. WS_2 thermally decomposes to W and S_2 at 1475 °C while more than
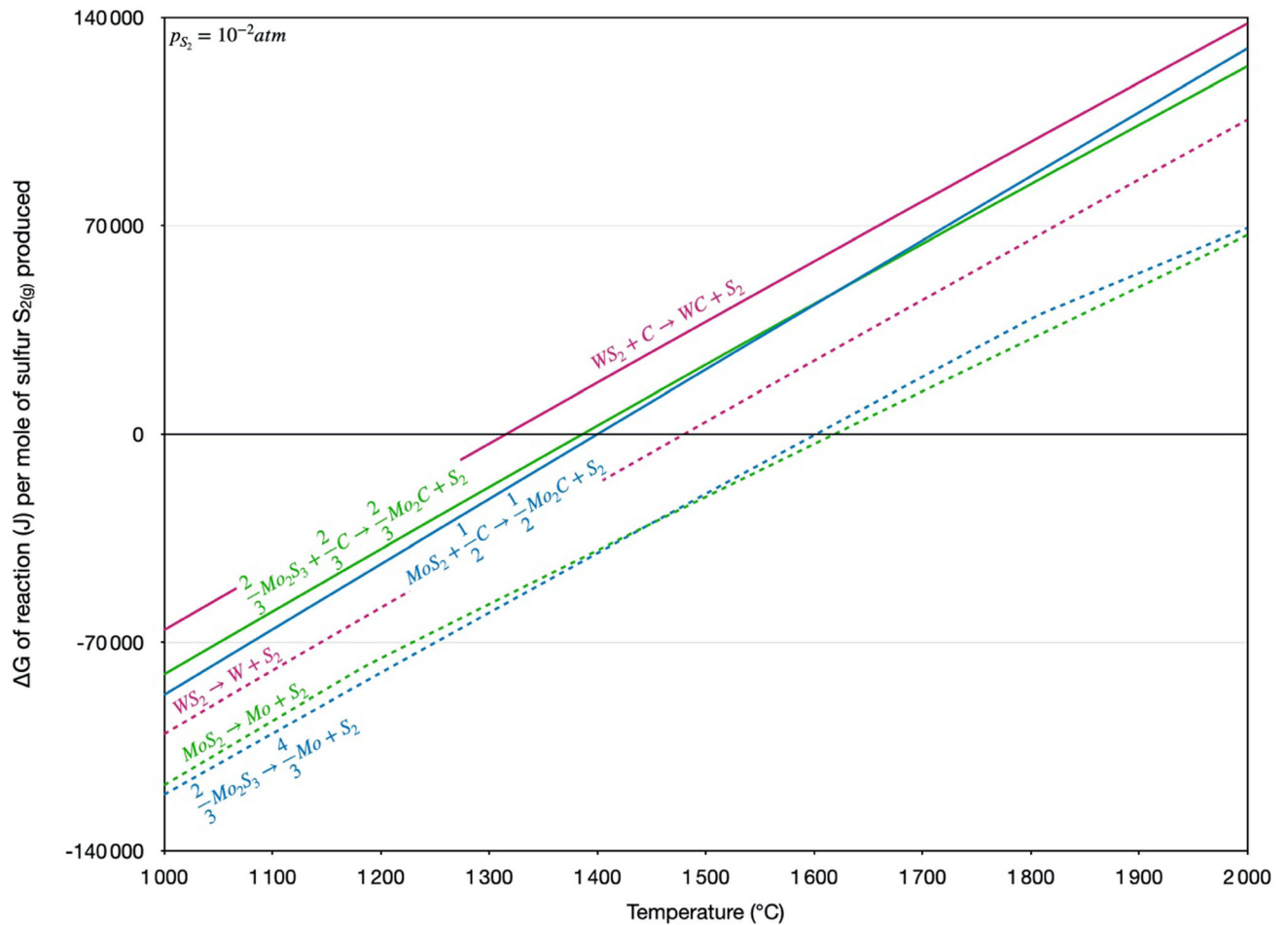
Fig. 16—Ellingham diagram of the thermal reduction and carburization of WS_2, MoS_2, and Mo_2S_3 for a partial pressure of $S_{2(g)}$ equals to 10^{-2} atm.

$1600\,°C$ is required for the decomposition of MoS_2 and Mo_2S_3. Interestingly, thermodynamically, the bi-carbide Mo_2C is more stable than MoC while W_2C is less stable than WC for a partial pressure of S_2 of 10^{-2} atm.

Regarding metallic tungsten production, a C-free crucible that would support the thermal decomposition remains to be found. A tungsten crucible can be used if the contact between the powder and the crucible is not too long to prevent the sintering of the tungsten particles on the crucible. Alumina crucible has been tested herein, but aluminum contamination (up to about 1 wt pct by EDS analysis) was found in the tungsten particles. Sintered rods as used herein do not need a floating-zone furnace to be decomposed to tungsten metal and can be processed in conventional furnaces.

Regarding tungsten carbide formation, the addition of graphite powder in the sulfidized powder could support the formation of WC and prevent the formation of W_2C. As discussed earlier, the formation of WC is thermodynamically more favorable than W_2C.

H. Discussion on the Physical Separation and Refining

Figure 14 suggests a broad size distribution of tungsten particles, from less than a micron up to several tens of microns. Physical separation and recovery of the particles by froth flotation are possible if the product particle size distribution can be narrowed. Particularly interesting results for the recovery of particles sized up to only few microns have been published.[49,50] However, as described by Chipfunhu et al.,[51] the froth recovery efficiency is highly dependent on the flotation reagents, particle size, and size distribution, hydrophobicity of particles, and other operating conditions.

Other possible physical separation techniques encompass sieving, centrifugal gravimetry,[52] electromagnetic[53] or electrostatic separation. These techniques are commonly used in ore beneficiation and need to be adapted for the recovery of the tungsten particles, considering the adequate separation technique for a specific particle size distribution.[54]

The thermodynamic and experimental results presented herein suggest a range of experimental parameters for optimization, to allow coarsening or a refined particle size distribution that would support the optimization of tungsten metal physical recovery.

From Table II, oxygen and sulfur represent a large fraction of the impurities of the metallic tungsten particles. Chemical analysis *via* ICP-AES and LECO post-physical separation would be necessary to determine, with precision, the level of impurities in both the metallic and carbide forms of tungsten. The EDS/WDS results presented herein suggest that the products obtained herein did not reach commercial purity.[1] The optimization of the sulfidation parameters remains to be conducted to evaluate how to lower the oxygen content.

Hydrogen reduction could be used to further purify the particles by production of H_2O and H_2S. The amount of hydrogen required would be function of the initial purity of the product resulting from sulfidation. Therefore, a complete reduction in the sense of complete oxygen removal (no oxygen diluted in sulfide phases) is preferred but not necessary. Further refining of the tungsten is also possible during the sintering process,[55] or even by electron beam melting.[56]

IV. CONCLUSION

New chemical and thermal pathways to produce tungsten sulfide, metallic tungsten, and tungsten carbide powders were demonstrated herein. The sulfidation of both wolframite and scheelite demonstrates high yields and the removal of some initial impurities such as tin. The sulfidation of wolframite and scheelite formed a mix of sulfides containing WS_2. Limitations for the sulfidation of scheelite are observed and some oxygen remains in both sulfidized powders with highest sulfidation yield, even though to a much lower extent for wolframite. A smaller particle size is expected to improve greatly the yield of scheelite sulfidation. We note that the tungstate compound $(WO_4)^{2-}$ exhibits a $6+$ tungsten valence while WS_2 involves a $4+$ tungsten valence. Sulfide compounds may offer a unique method to alter cation valences vis-à-vis the other chalcogens.

The actual experimental set-up for thermal reduction does not allow measurement of the partial pressure of sulfur. Tungsten sulfide selective reduction allowed for metallic tungsten particles production and our experimental conditions demonstrated that a partial pressure of sulfur of 10^{-2} atm is expected as the thermal decomposition happens around 1500 °C. Similar reasoning holds for tungsten carbide production. Discussion on the molybdenum impurities, physical separation, and refining was presented, suggesting potential opportunities for further utility of a sulfidation route for tungsten production.

ACKNOWLEDGMENTS

AUTHOR CONTRIBUTIONS

CB and SRG conducted the research conceived with advising from AA. CB wrote the manuscript with edits from AA. All authors reviewed the manuscript.

COMPETING INTERESTS

The authors declare no competing interests.

APPENDIX

See Tables AI and AII.

Table AI. Decomposition Reactions of Tungsten Sulfide, Calcium Sulfide, Iron Sulfide, and Manganese Sulfide in Function of Temperature

Thermal Range (°C)	Reaction
1000–2000	$WS_{2(s)} \rightarrow W_{(s)} + S_{2(g)}$
1000–1500	$2CaS_{(s)} \rightarrow 2Ca_{(s)} + S_{2(g)}$
1500–2000	$2CaS_{(s)} \rightarrow 2Ca_{(g)} + S_{2(g)}$
1000–1189	$2FeS_{(s)} \rightarrow 2Fe_{(s,\alpha)} + S_{2(g)}$
1190–1394	$2FeS_{(l)} \rightarrow 2Fe_{(s,\alpha)} + S_{2(g)}$
1394–1538	$2FeS_{(l)} \rightarrow 2Fe_{(s,\beta)} + S_{2(g)}$
1539–2000	$2FeS_{(l)} \rightarrow 2Fe_{(l)} + S_{2(g)}$
1000–1088	$2MnS_{(s)} \rightarrow 2Mn_{(s,\alpha)} + S_{2(g)}$
1089–1139	$2MnS_{(s)} \rightarrow 2Mn_{(s,\beta)} + S_{2(g)}$
1139–1245	$2MnS_{(s)} \rightarrow 2Mn_{(s,\gamma)} + S_{2(g)}$
1246–1530	$2MnS_{(s)} \rightarrow 2Mn_{(l)} + S_{2(g)}$
1530–2000	$2MnS_{(l)} \rightarrow 2Mn_{(l)} + S_{2(g)}$

The data have been obtained by FactSage 8.0 using the FactPS database. All partial pressures $(p_{S_{2(g)}}, p_{Ca(g)})$ equal 1 atm.

Table AII. Carburization Reaction Series of Tungsten Sulfide, Calcium Sulfide, Iron Sulfide, and Manganese Sulfide in Function of Temperature

Thermal Range (°C)	Reaction
1000–2000	$WS_{2(s)} + C_{(s)} \rightarrow WC_{(s)} + S_{2(g)}$
1000–2000	$WS_{2(s)} + \frac{1}{2}C_{(s)} \rightarrow \frac{1}{2}W_2C_{(s)} + S_{2(g)}$
1000–2000	$2CaS_{(s)} + 4C_{(s)} \rightarrow 2CaC_{2(s)} + S_{2(g)}$
1000–1189	$2FeS_{(s)} + \frac{2}{3}C_{(s)} \rightarrow \frac{2}{3}Fe_3C_{(s)} + S_{2(g)}$
1190–2000	$2FeS_{(l)} + \frac{2}{3}C_{(s)} \rightarrow \frac{2}{3}Fe_3C_{(s)} + S_{2(g)}$
1000–1530	$2MnS_{(s)} + \frac{2}{3}C_{(s)} \rightarrow \frac{2}{3}Mn_3C_{(s)} + S_{2(g)}$
1530–2000	$2MnS_{(l)} + \frac{2}{3}C_{(s)} \rightarrow \frac{2}{3}Mn_3C_{(s)} + S_{2(g)}$
1000–1530	$2MnS_{(s)} + \frac{6}{7}C_{(s)} \rightarrow \frac{2}{7}Mn_7C_{3(s)} + S_{2(g)}$
1530–2000	$2MnS_{(l)} + \frac{6}{7}C_{(s)} \rightarrow \frac{2}{7}Mn_7C_{3(s)} + S_{2(g)}$

The data have been obtained by FactSage 8.0 using the FactPS database. The partial pressure of $S_{2(g)}$, $pS_{2(g)}$, equals 1 atm.

REFERENCES

1. J.R.L. Trasorras, T.A. Wolfe, W. Knabl, C. Venezia, R. Lemus, E. Lassner, W.-D. Schubert, E. Lüderitz, and H.-U. Wolf: in *Ullmann's Encyclopedia of Industrial Chemistry*, Wiley-VCH Verlag GmbH & Co. KGaA, Weinheim, 2016, pp. 1–53.
2. K.B. Shedd: U.S. Geological Survey, Mineral Commodity Summaries, Tungsten, 2021, pp. 1–2.
3. E. Lassner, W.-D. Schubert, E. Lüderitz, and H.U. Wolf: in *Ullmann's Encyclopedia of Industrial Chemistry*, Wiley-VCH Verlag GmbH & Co. KGaA, 2012, vol. 37, pp. 497–536.
4. V. Zbranek, Z. Zbranek, and D.A. Burnham: US Patent 4092400, 1978.
5. W.-D. Schubert and E. Lassner: *Refract. Met. Hard Mater.*, 1991, vol. 10, pp. 133–41.
6. S. Omole, A. Lunt, S. Kirk, and A. Shokrani: *J. Manuf. Mater. Process.*, 2022, vol. 6(15), pp. 1–36.
7. J.W. Pugh and L.H. Amra: *J. Electrochem. Soc.*, 1960, vol. 107(12), pp. 990–93.
8. H. Tulhoff: in *Ullmann's Encyclopedia of Industrial Chemistry*, vol. 6, Wiley-VCH Verlag GmbH & Co. KGaA, Weinheim, 2012, pp. 565–82.
9. A. Tschinkowitz: Thesis: *Untersuchungen zur Karburierung grober Wolframpulver*, 1989.
10. E.J. Rees, C.D.A. Brady, and G.T. Burstein: *ScienceDirect Mater. Lett.*, 2008, vol. 62, pp. 1–3.
11. E.N. Kuzmichev, S.V. Nikolenko, and D.I. Balakhonov: *Theoret. Found. Chem. Eng.*, 2018, vol. 52(4), pp. 619–23.
12. J. Eckhart, J. Leitner, and K. Rabitsch: US Patent 20070036708A1, 2007.
13. C. Stinn and A. Allanore: *Nature*, 2022, vol. 602, pp. 78–83.
14. C. Stinn and A. Allanore: in *Ni-Co 2021: The 5th International Symposium on Nickel and Cobalt, Minerals, Metals and Materials Series*, 2021, pp. 99–110.
15. K.E. Daehn, C. Stinn, L. Rush, E. Benderly-Kremen, M.E. Wagner, C. Boury, B. Chmielowiec, C. Gutierrez, and A. Allanore: *Metals*, 2022, vol. 12(1440), pp. 1–25.
16. C. Stinn and A. Allanore: in *Rare Metal Technology 2022*, The Minerals, Metals & Materials Society, 2022, pp. 259–78.
17. S. Ahmad, M.A. Rhamdhani, M.I. Pownceby, and W.J. Bruckard: *Trans. Inst. Min. Metall. Sect. C*, 2014, vol. 123, pp. 165–77.
18. Y. Li, J.K. Wang, C. Wei, C.X. Liu, J.B. Jiang, and F. Wang: *Miner. Eng.*, 2010, vol. 23, pp. 563–66.
19. T. Zhang, W. Liu, J. Han, G. Wu, F. Jiao, and W. Qin: *Sep. Purif. Technol.*, 2021, vol. 259, p. 118064.
20. Y.-X. Zheng, W. Liu, W.Q. Qin, Y. Kong, H.-L. Luo, and J.-W. Han: *Sep. Sci. Technol.*, 2014, vol. 49, pp. 783–91.
21. Y.-X. Zheng, W. Liu, W.-Q. Qin, J.-W. Han, K. Yang, H.-L. Luo, and D.-W. Wang: *Can. Metall. Q.*, 2015, vol. 54, pp. 92–100.
22. J. Han, W. Liu, D. Wang, F. Jiao, and W. Qin: *Metall. Mater. Trans. B*, 2016, vol. 47B, pp. 344–54.
23. T. Kaneko, Y. Yashima, E. Ahmadi, S. Natsui, and R.O. Suzuki: *J. Solid State Chem.*, 2020, vol. 285, p. 121268.
24. P. Afanasiev, L. Fischer, F. Beauchesne, M. Danot, V. Gaborit, and M. Breysse: *Catal. Lett.*, 2000, vol. 64, pp. 59–63.
25. B. Zhang, L. Zhu, W. Liu, J. Han, F. Jiao, and W. Qin: *Metall. Mater. Trans. B*, 2019, vol. 50B, pp. 761–71.
26. E. Ahmadi and R.O. Suzuki: *Metall. Mater. Trans. B.*, 2020, vol. 51B, pp. 140–48.
27. Z. Zeng, B.Z. Dlugogorski, and M. Altarawneh: *Fire Saf. J.*, 2017, vol. 91, pp. 226–34.
28. F. Aliyu, M. Al-shaboti, Y. Garba, T. Sheltami, A. Barnawi, and M.A. Morsy: *Procedia Comput. Sci.*, 2015, vol. 63, pp. 499–504.
29. W.J. Schutte, J.L. De Boer, and F. Jellinek: *J. Solid State Chem.*, 1987, vol. 70, pp. 207–10.
30. E. Makovicky: in *Reviews in Mineralogy and Geochemistry*, J.J. Rosso, eds., 2006, vol. 61, Chap. 2, pp. 7–125.
31. C. Boury and A. Allanore: *Sci. Rep.*, 2021, vol. 11, p. 18189.
32. C. Stinn, S. Toll, and A. Allanore: in *Light Metals 2022, The Minerals, Metals & Materials Society*, 2022, pp. 681–88.
33. W. Zhang, Y. Zhou, J. Zhu, and Y. Pan: *Ind. Eng. Chem. Res.*, 2014, vol. 53, pp. 5646–41.
34. S. Ahmad, M.A. Rhamdhani, M.I. Pownceby, and W.J. Bruckard: *Metall. Mater. Trans. B*, 2015, vol. 46B, pp. 557–67.
35. H.Y. Sohn and S.E. Perez-Fontes: *Metall. Mater. Trans. B*, 2010, vol. 41B, pp. 1261–67.
36. H.Y. Sohn: *Metall. Trans. B*, 1978, vol. 9B, pp. 89–96.
37. D.A. Umbsaar and S.M. Antao: *Minerals*, 2022, vol. 12(42), pp. 1–12.
38. H. Cid-Dresdner and C. Escobar: *Z. Kristallogr.*, 1968, vol. 127, pp. 61–72.
39. St. Knitter and M. Binnewies: in *Zeitschrift für anorganische und allgemeine Chemie*, 1999, vol. 625, pp. 1582–88.
40. J. Cho and H.Y. Sohn: *Can. J. Chem. Eng.*, 2016, vol. 94, pp. 1516–23.
41. H.Y. Sohn: *Can. J. Chem. Eng.*, 2019, vol. 97, pp. 2061–67.
42. M. Ishida and C.Y. Wen: *AlChE J.*, 1968, vol. 14(2), pp. 311–17.
43. H.Y. Sohn and H.-J. Sohn: *Ind. Eng. Chem. Process. Des. Dev.*, 1980, vol. 19, pp. 237–42.
44. L.M. Tavares and R.P. King: *Int. J. Miner. Process.*, 1998, vol. 54, pp. 1–28.
45. F.K. Crundwell, M.S. Moats, V. Ramachandran, T.G. Robinson, and W.G. Davenport: in *Extractive Metallurgy of Nickel, Cobalt and Platinum Group Metals*, F.K. Crundwell, M.S. Moats, V. Ramachandran, T.G. Robinson, and W.G. Davenport, eds., Elsevier, Oxford, 2011, pp. 95–107.
46. Z. Zhao, C. Cao, X. Chen, and G. Huo: *Hydrometallurgy*, 2011, vol. 108, pp. 229–32.
47. M.H.H. Mahmoud, S. Nakamura, and K. Akiba: *Solvent Extr. Ion Exch.*, 1996, vol. 14(2), pp. 203–17.
48. Y. Zeng, A.C. Domask, and S.E. Mohney: *Mater. Sci. Eng. B*, 2016, vol. 212, pp. 78–88.
49. J.D. Pease, D.C. Curry, and M.F. Young: *Miner. Eng.*, 2006, vol. 19, pp. 831–40.
50. J.D. Pease, M.F. Young, D. Curry, and N.W. Johnson: *Trans. Inst. Min. Metall. Sect. C*, 2010, vol. 119(4), pp. 216–22.
51. D. Chipfunhu, G. Bournival, S. Dickie, and S. Ata: *Miner. Eng.*, 2019, vol. 131, pp. 272–79.
52. Q. Dehaine, Y. Foucaud, J.S. Kroll-Rabotin, and L.O. Filippov: *Sep. Purif. Technol.*, 2019, vol. 215, pp. 590–601.
53. S. Farrokhpay, L. Filippov, and D. Fornasiero: *Miner. Eng.*, 2019, vol. 141, p. 105892.
54. G. Dermont, M. Bergeron, G. Mercier, and M. Richer-Laflèche: *J. Hazard. Mater.*, 2008, vol. 152, pp. 1–31.
55. J.L. Johnson: in *Sintering of Advanced Materials*, Z. Zak Fang, ed., Woodhead Publishing, 2010, Chap. 14, pp. 356–88.
56. L. Long, W. Liu, Y. Ma, Y. Liu, and S. Liu: *High Temp. Mater. Process.*, 2015, vol. 34, pp. 605–10.